Open Access

Recent Progress in Materials

LIDSEN Publishing Inc.

Original Research

Elastohydrodynamic Squeeze-film Interaction in Synovial Joints with Nanofluid Lubrication

Mohammad Yaghoub Abdollahzadeh Jamalabadi *

Department of Marine Engineering, Chabahar Maritime University, Chabahar, Iran; E-Mail: My.Abdollahzadeh@cmu.ac.ir

* **Correspondence:** Mohammad Yaghoub Abdollahzadeh Jamalabadi; E-Mail: My.Abdollahzadeh@cmu.ac.ir

Academic Editor: Krzysztof Wierzcholski

Special Issue: Non-Conventional Hydrodynamic Lubrication for Biological and Mechanical Surfaces

Recent Progress in Materials
2022, volume 4, issue 4
doi:10.21926/rpm.2204021

Received: July 09, 2022
Accepted: September 30, 2022
Published: October 19, 2022

Abstract

New lubrication events can be predicted using improved pathological non-Newtonian physiological fluids coupled to phospholipid-based bilayers in variable time-dependent magnetic fields under random non-steady conditions. In this study, we investigated nanofluid lubrication systems for synovial joints. The particles of PSPMA-g-HSNPs were used as nanoparticles. The hydrodynamic interaction between the knee bones separated by a nanofluid film was considered here for various nanofluid concentrations. The simulation indicated solid mechanics on the bones being pushed by 45 kg-force. The lubricant layer was squeezed by the approaching bones, which increased the pressure on the lubricant. The calculated maximum lubricant pressure and the change in film height with time were compared to analytical solutions. The results showed that the application of the nanofluid technology on non-conventional lubrication systems for synovial joints was feasible. Finally, we also found that with an increase in the nanoparticle concentration, the maximum pressure on the squeeze film decreased, which introduced a new type of bio-fluid to non-conventional lubrication systems for synovial joints.

Keywords
Nonlinear; synovial joints; risk assessment; elastohydrodynamic; Reynolds theory

1. Introduction

Biological surfaces move relative to each other using a water-based mechanism. Hence, various strategies are needed to maintain uniform wear or friction [1]. Mechanical components wear and tear due to friction when they are not lubricated [2]. Lubricants and elastic bodies make elastohydrodynamic contacts [3]. Such elastohydrodynamic interactions cause mechanical stress near the contact center and increase the pressure in the lubricant [4]. Hydrodynamic problems are solved numerically by using Reynold's equation coupled with solid mechanics to model the elastohydrodynamic interaction [5]. The schematic representations of the problem from the front, side, and top views are shown in Figure 1. The curvilinear lines depicted on the bone surface near the point of contact shown in Figures 1a, 1b, and 1c denote the normal mesh on the geometry. Several studies have been conducted on these approaches in the last few years. We conducted this study focusing on the synovial joints and the mouth.

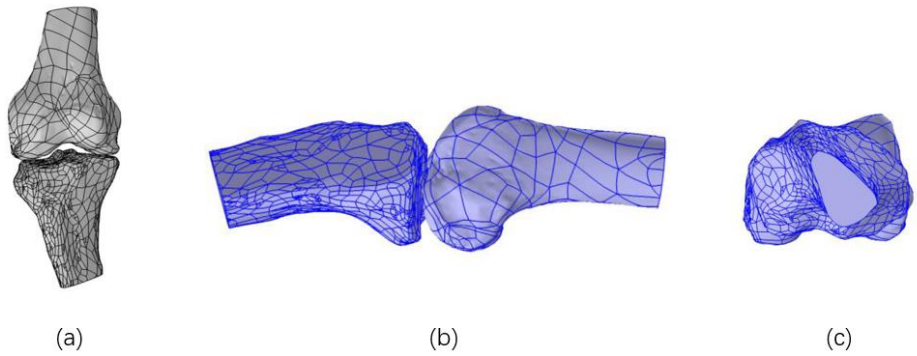

Figure 1 Schematic representation of the problem: (a) front view, (b) side view, and (c) top view.

Cartilage is a white connective tissue composed of chondrocytes. An articular cartilage layer in human joints varies in thickness from 0.5 to 1.5 mm in the joints of the upper extremity, such as the hand and shoulder, and from 1 to 6 mm in the joints of the lower extremity, such as the hip, knee, and ankle. Under normal conditions, the articular cartilage provides a low level of friction and wear. The porosity of adult joints varies from 68 to 85%, and it is a highly hydrated tissue. There are electrolytes, such as sodium and chloride, in the interstitial fluid of cartilage. A method of ultrasonic matching layer measurement was described in some studies for measuring viscosity in situ in an operating journal bearing [6]. Ultrasonic viscometers mounted on journals were used to measure circumferential viscosity [7]. Four viscosity regions were identified based on the results and included a low-temperature and no load, a high-temperature and load, a maximum load and temperature, and a high-temperature and no load [8]. These viscosity regions matched the viscosity field expected by superimposing the temperature and pressure gradients [9]. By quantifying the loss of power in

the bearing, the viscosity results became even more valuable [10]. In the small area where the film thickness was minimum, and the load was maximum, most of the losses were localized. Simulations of journal-bearing hydrodynamic lubrication were compared to experimental results [11]. According to the results of the comparison between the ultrasonic viscometer and the model, the maximum load occurs at the same angle and loaded region. Because the numerical model does not take thermal effects and shear heating into account, the maximum viscosity measured with the numerical model is different from that obtained by using viscometers [12]. The findings of this study might contribute significantly to the advancement of the automotive and lubricant industries. They also might provide a deeper understanding of the complex lubrication conditions present in engine contacts and strengthen the validity of existing lubrication models [13].

Alzahrani et al. [14] investigated the flow of micropolar fluids over a unique form of vertical stretching sheet. They focused on studying temperature-dependent properties. Gao et al. investigated the effects of various initial temperature and pressure conditions to predict the thermal conductivity and the duration of phase alteration of water-based carbon hybrid nanofluids based on the MD approach. [15]. They found that the initial condition plays an important role. Human and Ecological Risk Assessment of a new type of textile was investigated by Mahmood et al. [16]. They investigated the bioremediation of textile industrial effluents by Fomitopsis Pinicola IEBL-4 for environmental sustainability. Nayak et al. [17] studied the nonlinear radiative flow of hybrid nanofluids. The system was optimized based on entropy. Qi et al. [18] studied extended surfaces during the melting and freezing of phase-changing materials in cylindrical lithium-ion battery cooling. They optimized the system and performed a sensitivity analysis. Ramadan et al. [19] studied the thermal creep effects on fluid flow and heat transfer via microchannel gas heating. Due to thermal creep, gas temperatures increase in the developing region, and the exchange of fluids and wall heat increases at the entrance. Increasing the Knudsen numbers intensifies the thermal creep effect significantly on gas-to-wall heat exchange. Tlili and Alharbi [20] studied the effect of changing the air quality and stream incident on the Trombe wall for two different arrangements of rectangular blocks of phase change materials in the wall. On cold days, solar sources can reduce energy consumption (EC) for buildings, but in the summer, they increase EC. Tlili et al. [21] conducted a flat sheet direct contact membrane distillation study to decrease the energy demand for solar desalination. Solar energy was better utilized by using two techniques in their study. Zhang et al. [22] investigated the effects of Al_2O_3 and TiO_2 nanoparticles to reduce the energy demand in conventional buildings by integrating solar collectors and phase change materials. The effects of Brownian motion on the activity of nanoparticles were discussed in some studies [23, 24] but neglected in this study.

This study might contribute to the development of advanced lubricant formulations by providing numerical techniques and fundamental knowledge. We investigated the elastohydrodynamic squeeze-film interaction in synovial joints with nanofluid lubrication and presented the benefits of the new lubricant.

2. Mathematical Model

As an extension to the knee case, this study included elastic deformation and stress on the contacting wall. This occurs when a solid joint interacts with a wall separated by a lubricant film. In the model, an external force was applied to push a solid knee toward a solid knee wall. As the knee approached, the lubricant layer was squeezed, increasing its pressure. The analytical solutions were

compared to the calculated maximum lubricant pressure and film height over time. The fluid continuity was evaluated using Equation (1):

$$\nabla.\mathbf{v} = 0 \tag{1}$$

Here, v denotes the velocity of the lubricant [m/s]. Equation (1) is related to the stationary flow of bio-fluids around the bones in the joint. This equation is valid only for incompressible and time-independent fluids but not valid for the compressible and time-depended (non-stationary) fluids and squeeze films, which are described in this study. Assuming fully flooded conditions, laminar flow, Newtonian rheology, smooth surfaces, and an isothermal steady-state regime, the lubricant equation can be expressed as:

$$\nabla.(\rho_{fluid}\mathbf{v}) = \frac{\partial}{\partial t}(\rho_{fluid}) \tag{2}$$

Here, ρ_{fluid} denotes the density of the fluid [kg/m^3]. For non-slip boundary conditions at the wall and the base, the Reynolds equation can be expressed as:

$$\frac{\partial}{\partial t}(\rho_{fluid}h) = \nabla_t \cdot (\rho_{fluid}h\mathbf{v}_{ave}) \tag{3}$$

Here, ∇_t denotes the tangential temperature gradient and results from the difference between the gradient and its normal projection ($\nabla - (\boldsymbol{n}.\nabla)\boldsymbol{n}$). Nabla vectors ∇ and ∇_t have a unit of 1/m. For non-slip boundary conditions at the wall and the base, the Reynolds equation can be expressed as Eq. (3) where $\mathbf{v}_{ave}$ denotes the average velocity of the lubricant relative to the top and bottom surfaces [m/s] and can be calculated using Equation (4).

$$\mathbf{v}_{ave} = \frac{1}{2}(\mathbf{v}_{w,t} + \mathbf{v}_{b,t}) - \frac{h^2}{12\mu}\nabla_t p_f \tag{4}$$

Here, μ denotes the viscosity, p_f (a dependent variable) denotes the pressure developed because of the flow, and h denotes the film thickness, which can be evaluated using Equation (5).

$$h = h_w + h_b \tag{5}$$

with two components separated by a reference surface between wall and base with the name of the wall height

$$h_w = h_{w1} - \mathbf{u}_w \cdot \mathbf{n}_{\text{ref}} - \mathbf{u}_w \cdot \nabla_t h_{w1} \tag{6}$$

and base height

$$h_b = h_{b1} + \mathbf{u}_b \cdot \mathbf{n}_{\text{ref}} - \mathbf{u}_b \cdot \nabla_t h_{b1}. \tag{7}$$

The normal orientation of the reference surface is from the wall to the base surfaces (z from -h_b to h_w). When modeling the laminar flow in thin gaps or channels, the total gap height is assumed to be considerably smaller than the typical lateral dimension of the reference surface. The height of the wall above the reference surface (h_w) and the height of the base below the reference surface

(h_b) are determined by the components of h_{w1} and h_{b1}, which are the initial distances to the wall and base, respectively. The Eulerian wall height changes from an initial value of h_{w1} to a final value of h_w. The geometrical localization of u_w, n_{ref}. h_w, and h_b are shown in Figure 2a. To determine the geometrical parameters shown in the figures that were present in the system, a schematic representation of the orientation of the wall and the base surfaces associated with the reference surface in the thin-film flow was depicted. A vector from the reference surface to the corresponding point on the wall always points in the $-\mathbf{n}_{ref}$ direction, where $\mathbf{n}_{ref}$ is the reference surface normal. Similarly, a vector from the reference surface to the corresponding point on the base points in the $+\mathbf{n}_{ref}$ direction. The height of the wall above the reference surface (h_w) and the height of the base below the reference surface (h_b) are also shown in the figure. The geometrical localization of u_w and v_w are shown in Figure 2b. The displacement of the wall and the base from the reference surface, and the corresponding change in the height of the channel are shown in Figure 2b.

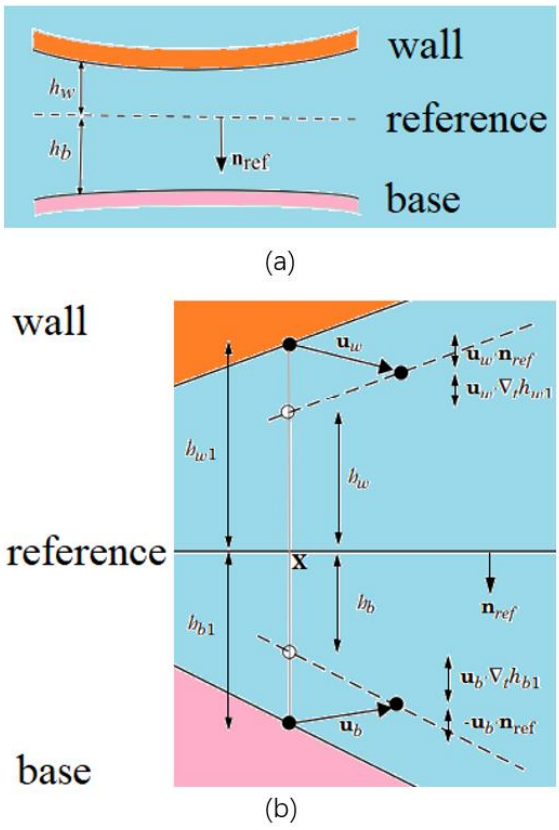

Figure 2 (a) A schematic representation of the orientation of the wall and the base surfaces with respect to the reference surface in the thin-film flow. A vector from the reference surface to the corresponding point on the wall always points in the $-\mathbf{n}_{ref}$ direction, where $\mathbf{n}_{ref}$ is the reference surface normal. Similarly, a vector from the reference surface to the corresponding point on the base points in the $+\mathbf{n}_{ref}$ direction. The height of the wall above the reference surface (h_w) and the height of the base below the reference surface (h_b) are also shown in the figure. (b) The displacement of the wall and the base with respect to the reference surface and the corresponding change in the height of the channel are shown.

Similarly, the base height changed from an initial value of h_{b1} to h_b. The absolute pressure (p_A) consisted of p_f (the pressure resulting from the fluid flow) and p_{ref} (the reference pressure level)

$$p_A = p_{ref} + p_f \tag{8}$$

The compression of the fluid resulted in an excess pressure above the reference pressure and a fluid velocity in the gap. The three-dimensional equilibrium bone solid material was modeled using Equation (9).

$$\rho_{solid} \frac{\partial^2 \mathbf{u}}{\partial t^2} = \text{Div}\, \mathbf{S}_{solid} + \mathbf{F}_{solid} \tag{9}$$

In the bone solid material tensor equation of the equilibrium bone material, **S** denotes the solid stress tensor [N/m**²**], **u** denotes the solid displacement vector [m], and **F** denotes body force [N/m**³**] (volume force). Each term in Equation (9) has a unit of [N/m**³**].

In Eq. (9), the proper constitutive relationships between stress tensor S_{solid} and strain tensor for hyper-elastic bone material were put. We substituted the geometrical relationships between strain tensor and covariant derivatives of the displacement vector components in the material of the bone.

A range of 0.29 to 0.63 was found for Poisson's ratio [25]. Here the value of 0.33 is used. The bone elastic modulus is considered 13 Gpa [26]. The tensor equation for the equilibrium of the lubricant liquid material with inertia forces, i.e., with nonlinear substantial terms, can be expressed as follows:

$$\rho_{fluid} \frac{d\mathbf{v}}{\text{dt}} = \nabla \mathbf{S}_{fluid} + \mathbf{F}_{fluid} \tag{10}$$

Here, **v** [m/s] denotes lubricant velocity vector (for bio liquid material), ρ_{fluid} [kg/m^3] denotes the lubricant density, $\mathbf{S}_{fluid}$ [Pa] denotes the stress tensor in the lubricant, and $\mathbf{F}_{fluid}$ [N/m^3] denotes the body force vector in the lubricant. In Eq. (10), the proper constitutive relationships between stress tensor S_{fluid} and strain (shear rate) tensor for non-Newtonian bio-lubricant were put. Next, we substituted the geometrical relationships between strain tensor (with shear rate components) and covariant derivatives of the bio-lubricant velocity vector components. The boundary condition of stress transfer across the fluid-solid surface was expressed by the quality of the pressure [Pa] at the boundary:

$$P_{fluid} = P_{solid} \tag{11}$$

The external force, **F**, is counterbalanced by the pressure in the lubricant and is imposed as a constraint. The behavior of lubricants under pressure is most significant when there are concentrated contacts (a large normal force over a small area, usually distorted). Barus showed how the lubricant viscosity varies with pressure at a constant temperature. The pressure field of the fluid was then used to predict the viscosity change in the fluid based on the Barus equation.

$$\eta = \eta_0 e^{\alpha p} \tag{12}$$

The Barrus formula in contemporary Bio-EHD scientific research (problem) is sufficient. The pressure viscosity coefficient α (0.01 mm^2/N) in the Barus equation is used to describe the variation of

viscosity with pressure. The pressure coefficient α in the Barrus formula was adjusted to the non-Newtonian bio-lubricant, and hence, depended not only on the pressure but also on the wettability in bio-contact and power hydrogen ion concentration (pH) of the bio-fluid. Both the roll and the strip surfaces were rough. The squeeze film models over the knee bone on the top bone, bottom bone, and the squeeze film boundary are shown in Figure 3. The curvilinear lines on the bone surface near the point of contact are shown in the squeeze film model in Figures 3a, 3b, and 3c. denoted the mesh divisions used here. The black areas in Figures 3a and 3b indicate a solid material of the bone, while the blue area is related to the squeeze film surface. The blue line in Figure 3c indicates the free surface of the pressure field in the squeeze film.

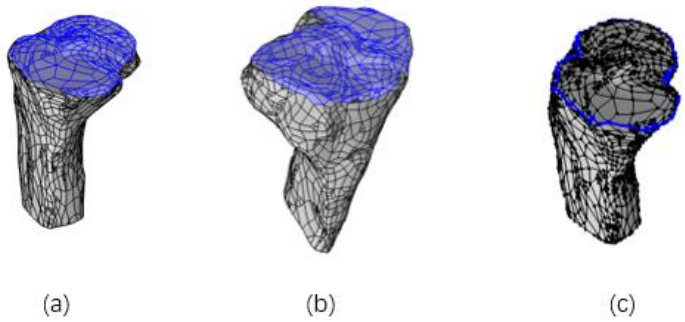

Figure 3 The squeeze film model over the (a) knee bone, (b) top bone, and (c) bottom bone squeeze film boundary.

3. Validation

A finite difference algorithm was used to compare the experimentally measured viscosity around the bearing circumference to the well-known analytical solution derived from a semi-iso-viscous Reynolds equation model for hydrodynamic lubrication of journal bearings. The construction of an elastohydrodynamic model of film formation and viscosity was beyond the scope of this study. We used a simplified approach to determine where the pressure variation in the bearing gap increases viscosity the most. The results of the data obtained from the experiments were then compared to this value. We provided a chart for calculating the bearing gap. The Raimondi-Boyd charts provide solutions for the Reynolds equation for different parameters (e.g., film thickness) for one-dimensional flow. The comparison between the calculated and analytical values of maximum change in film height is shown in Figure 4. The SI unit ([m]) used to plot the values of the maximum changes in film height is shown on the vertical axis of Figure 4.

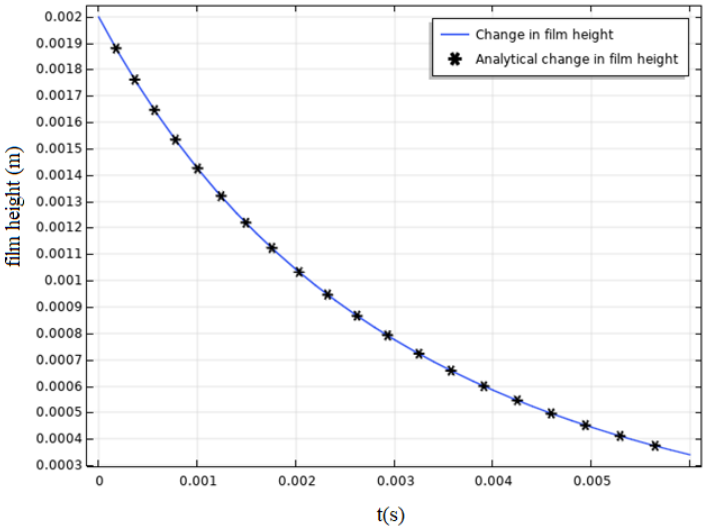

Figure 4 The comparison between the calculated and analytical values of the maximum change in film height.

4. Results and Discussion

The results of pressure measurements along the bearing circumference are shown in Figure 4. As shown in Figure 5a, four distinct pressure regions were identified. As shown in Figure 5b, these were visualized as uniform plots for the bone. The data were recorded at the corresponding bearing position when the pressure in the different zones was reported. The bar unit (1 bar = 100,000 Pa) is the pressure value shown on the vertical axis of Figure 5a. The pressure units are shown via the von Mises stress plots at the boundaries of the bone or cartilage elastic solid, as shown on the vertical axis of Figure 5b.

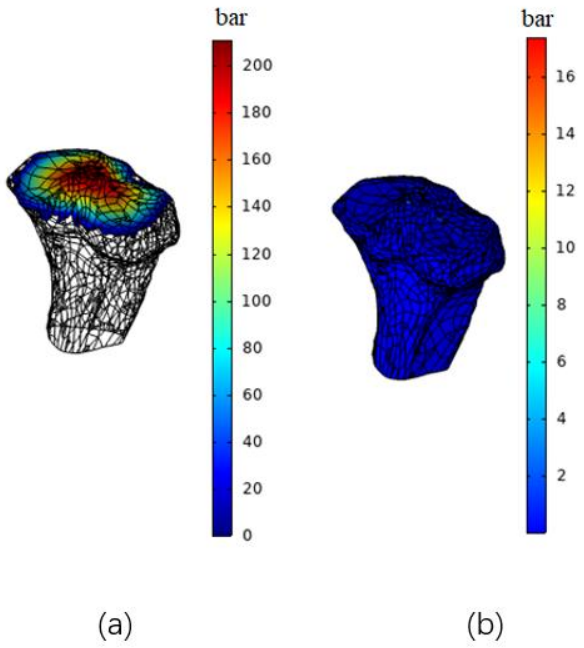

Figure 5 (a) The pressure distribution in the lubricant. (b) The von Mises stress plot at the boundaries of the elastic solid.

The synovial fluid (also called synovia) in the synovial joints is a non-Newtonian viscous fluid. The synovial fluid, which resembles the egg white, reduces friction between the articular cartilage and the synovial joints during movement. As a part of the extracellular fluid, the synovial fluid makes up a small component.

The lubrication in bionic joints cannot be explained by such specific mechanisms. To explain the tribology of bionic joints, all lubrication mechanisms are necessary, as shown in Figure 6. Bionic joints have an extremely low friction coefficient of 0.002, which is due to the interaction between the synovial fluid and the articular tissue. The bionic joint is lubricated by boundary lubrication mechanisms, especially during long periods of standing and heel strikes. The pressure (in Pa) is depicted on the vertical axis of Figure 6a. The maximum pressure (Pa) of a heel strike is plotted on the vertical axis of Figure 6b. In general, a gait cycle of one leg can be divided into a stance phase (60%) initiated by a heel strike and terminated by a toe-off and a swing phase (40%). During the stance phase, the knee flexion angle increases from 0° at heel strike to a maximum of 15°, while during the swing phase the flexion angle increases to approximately 60°.

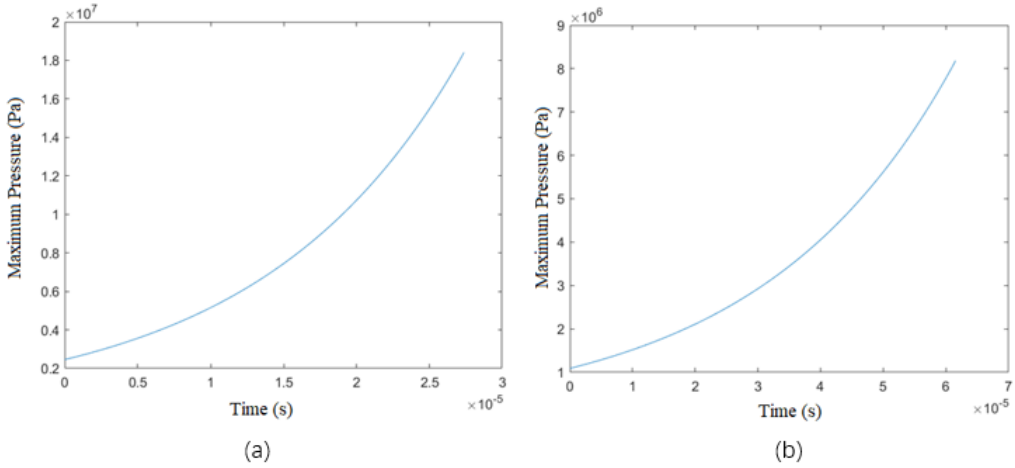

Figure 6 The maximum pressure was applied to the film for lubrication to describe the knee joint tribology (a) weight transfer and (b) heel strike.

The hollow silica nanoparticles with core/shell charged polymer brushes (PSPMA-g-HSNPs) were used here as nanoparticles. By using charged polymer brushes to form shells, the functional nanoparticles showed a positive lubricating effect in aqueous media via hydration lubrication. Under high stress, cartilage and menisci in the knee joint are elastically deformed. The elastohydrodynamic of the synovial fluid is the study of these elastic deformations related to the dynamics of that fluid. Biological Consider now the tribological behavior of the elastic cartilaginous tissue and meniscal tissue are pressed against a spherical condyle with the radius of curvature shown in the figure, in this case, the thickness of the synovial fluid film is calculated. The relationship between various nanofluid concentrations and the change in the film height and maximum pressure is shown in Figure 7. Various concentrations of PSPMA-g-HSNPs are shown in Figure 7. The change in the film height (in meters) and the maximum pressure (in pascal) are shown on the vertical axis of Figures 7a and 7b. Sub-atmospheric fluid pressure was present in every joint (mean –2.8 ±0.4 cm H_2O, in the elbow, and –5.7 ±0.3 cm H_2O, in the knee) and many other interstitial spaces. Approximately 40–46% of serum levels were represented by colloid osmotic pressure (mean 11.4 ±0.9 cm H_2O, in the shoulder,

and 13.1 ±1.0 cm H_2O, in the elbow). The mesoporous hollow silica cores of PSPMA-g-HSNPs facilitate drug-loading and release.

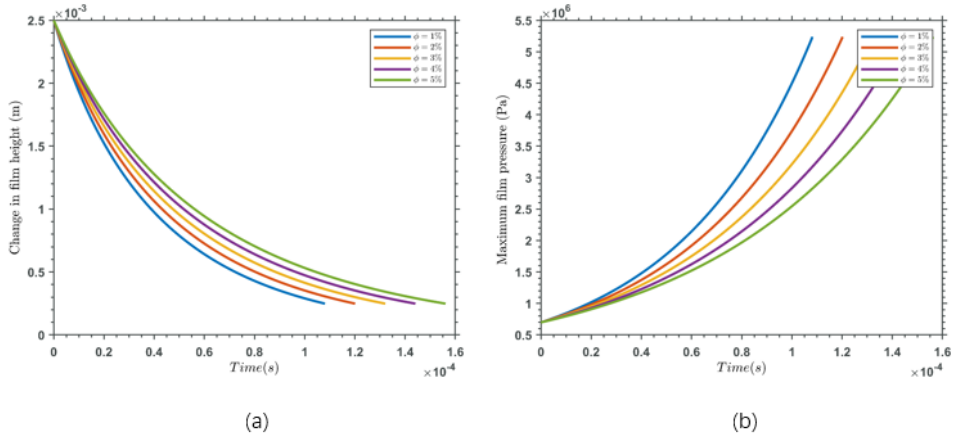

Figure 7 The relationship of various nanofluid concentrations with (a) the changes in the film height versus time and (b) the maximum pressure versus time.

5. Conclusion

In this study, we investigated protein film formation mechanisms in artificial hip joints. New lubrication events can be predicted using improved pathological non-Newtonian physiological fluids coupled to phospholipid-based bilayers in variable time-dependent magnetic fields under random non-steady conditions. In this study, we focused on nanofluid lubrication systems for synovial joints. The hydrodynamic interaction between the knee bones separated by a nanofluid film was considered here for various nanofluid concentrations. The simulation indicated solid mechanics on the bones being pushed by 45 kg-force. The lubricant layer was squeezed by the approaching bones, which increased the lubricant pressure. The calculated maximum lubricant pressure and the change in the film height with time were compared to analytical solutions. Our conclusions are listed below.

1. The results showed that the application of nanofluid technology on non-conventional lubrication systems for synovial joints was feasible.
2. Film formation obeys iso-viscous, incompressible fluid predictions.
3. An increase in time decreased the film height and increased the pressure.
4. An increase in the nanoparticle concentration decreased the maximum pressure on the squeeze film, which introduced a new type of bio-fluid in the non-conventional lubrication systems for synovial joints.
5. An increase in the nanoparticle concentration increased the film height on the squeeze film.

Author Contributions

The author did all the research work of this study.

Competing Interests

The author has declared that no competing interests exist.

References

1. Schirru M, Mills R, Dwyer-Joyce R, Smith O, Sutton M. Viscosity measurement in a lubricant film using an ultrasonically resonating matching layer. Tribol Lett. 2015; 60: 1-11.
2. Lamb J. Physical properties of fluid lubricants: Rheological and viscoelastic behaviour. Proc Inst Mech Eng. 1967; 182: 293-310.
3. Barlow AJ, Lamb J. The visco-elastic behaviour of lubricating oils under cyclic shearing stress. Proc R Soc Lond. 1959; 253: 52-69
4. Dowson DG, Higginson GR, Whitaker AV. Elasto-hydrodynamic lubrication: A survey of isothermal solutions. J Mech Eng Sci. 1962; 4: 121-126.
5. Johnson KL, Tevaarwerk JL. Shear behaviour of elastohydrodynamic oil films. Proc R Soc Lond. 1977; 356: 215-236.
6. Stachowiack GW, Batchelor AW. Engineering Tribology. 2nd ed. Oxford: Butterworth Heinemann; 2001.
7. Sun Y, Yan X, Yuan C, Bai X. Insight into tribological problems of green ship and corresponding research progresses. Friction. 2018; 6: 472-483.
8. Dong C, Yuan C, Bai X, Yang Y, Yan X. Study on wear behaviours for NBR/stainless steel under sand water-lubricated conditions. Wear. 2015, 332: 1012-1020.
9. Wang H, Liu Z, Zou L, Yang J. Influence of both friction and wear on the vibration of marine water lubricated rubber bearing. Wear. 2017; 376: 920-930.
10. Van Ostayen R, Van Beek A, Ros M. A mathematical model of the hydro–support: An Elasto-hydrostatic thrust bearing with mixed lubrication. Tribol Int. 2004; 37: 607-616.
11. Wodtke M, Olszewski A, Wasilczuk M. Application of the fluid–structure interaction technique for the analysis of hydrodynamic lubrication problems. Proc Inst Mech Eng J. 2013; 227: 888-897.
12. Wellauer E, Holloway G. Application of EHD oil film theory to industrial gear drives. J Eng Ind. 1976; 98: 626-631.
13. Cameron A. Basic lubrication theory. Harlow: Longman; 1971.
14. Alzahrani J, Vaidya H, Prasad KV, Rajashekhar C, Mahendra DL, Tlili I. Micro-polar fluid flow over a unique form of vertical stretching sheet: Special emphasis to temperature-dependent properties. Case Stud Therm Eng. 2022; 34: 102037. doi: 10.1016/j.csite.2022.102037.
15. Gao J, Liu J, Yue H, Zhao Y, Tlili I, Karimipour A. Effects of various temperature and pressure initial conditions to predict the thermal conductivity and phase alteration duration of water based carbon hybrid nanofluids via MD approach. J Mol Liq. 2022; 351: 118654. doi: 10.1016/j.molliq.2022.118654.
16. Mahmood RT, Asad MJ, Hadri SH, El-Shorbagy MA, Mousa AA, Dara RN, et al. Bioremediation of textile industrial effluents by Fomitopsis pinicola IEBL-4 for environmental sustainability. Hum Ecol Risk Assess. 2022: 1-18. doi: 10.1080/10807039.2022.2057277.
17. Nayak MK, Mabood F, Dogonchi AS, Ramadan KM, Tlili I, Khan WA. Entropy optimized assisting and opposing non-linear radiative flow of hybrid nanofluid. Waves Random Complex Media. 2022: 1-22. doi: 10.1080/17455030.2022.2032474.

18. Qi X, Sidi MO, Tlili I, Ibrahim TK, Elkotb MA, El-Shorbagy MA, et al. Optimization and sensitivity analysis of extended surfaces during melting and freezing of phase changing materials in cylindrical Lithium-ion battery cooling. J Energy Storage. 2022; 51: 104545. doi: 10.1016/j.est.2022.104545.
19. Ramadan KM, Kamil M, Tlili I, Qisieh O. Analysis of thermal creep effects on fluid flow and heat transfer in a microchannel gas heating. J Therm Sci Eng. 2021; 13: 061011. doi: 10.1115/1.4050236.
20. Tlili I, Alharbi T. Investigation into the effect of changing the size of the air quality and stream to the trombe wall for two different arrangements of rectangular blocks of phase change material in this wall. J Build Eng. 2022; 52: 104328.doi: 10.1016/j.jobe.2022.104328.
21. Tlili I, Sajadi SM, Baleanu D, Ghaemi F. Flat sheet direct contact membrane distillation study to decrease the energy demand for solar desalination purposes. Sustain Energy Technol Assess. 2022; 52: 102100. doi: 10.1016/j.seta.2022.102100.
22. Zhang J, Sajadi SM, Chen Y, Tlili I, Fagiry MA. Effects of Al_2O_3 and TiO_2 nanoparticles in order to reduce the energy demand in the conventional buildings by integrating the solar collectors and phase change materials. Sustain Energy Technol Assess. 2022; 52: 102114. doi: 10.1016/j.seta.2022.102114.
23. Abdollahzadeh Jamalabadi MY, Park JH. Effects of Brownian motion on freezing of PCM containing nanoparticles. Therm Sci. 2016; 20: 1533-1541.
24. Abdollahzadeh Jamalabadi MY. MD simulation of Brownian motion of Buckminsterfullerene trapping in nano-Optical Tweezers. Int J Opt Appl. 2015; 5: 161-167.
25. Reilly DT, Burstein AH. The elastic and ultimate properties of compact bone tissue. J Biomech. 1975; 8: 393-405.
26. Peters AE, Akhtar R, Comerford EJ, Bates KT. The effect of ageing and osteoarthritis on the mechanical properties of cartilage and bone in the human knee joint. Sci Rep. 2018; 8: 5931.